Chinese Chemical Letters 36 (2025) 110108

Contents lists available at ScienceDirect

Chinese Chemical Letters

journal homepage: www.elsevier.com/locate/cclet

A short review on research progress of $ZnIn_2S_4$-based S-scheme heterojunction: Improvement strategies

Hongrui Zhang[a], Miaoying Cui[a], Yongjie Lv[a], Yongfang Rao[a,*], Yu Huang[b,c]

[a] *Department of Environmental Science and Engineering, Xi'an Jiaotong University, Xi'an 710049, China*
[b] *Key Laboratory of Aerosol Chemistry and Physics, State Key Laboratory of Loess and Quaternary Geology (SKLLQG), Institute of Earth Environment, Chinese Academy of Sciences, Xi'an 710061, China*
[c] *Center of Excellence in Quaternary Science and Global Change, Chinese Academy of Sciences, Xi'an 710061, China*

ARTICLE INFO

Article history:
Received 17 March 2024
Revised 25 April 2024
Accepted 11 June 2024
Available online 12 June 2024

Keywords:
Photocatalysis
$ZnIn_2S_4$
S-scheme
Heterojunction
Improvement strategies

ABSTRACT

$ZnIn_2S_4$, a typical n-type semiconductor, has received intensive attention due to its suitable bandgap, excellent visible light absorption performance, and simple and flexible preparation methods. However, its application is curbed by photo-generated carrier recombination and photo corrosion. Although constructing S-scheme heterojunctions by combining $ZnIn_2S_4$ with other semiconductors can solve these problems, the photocatalytic activity of S-scheme heterojunctions can be further improved. Therefore, this short review summarizes modification strategies of $ZnIn_2S_4$-based S-scheme heterojunctions. This article also introduces the concept, design principles, and characterization methods of $ZnIn_2S_4$-based S-scheme heterojunction. Finally, current challenges and future research focuses related to $ZnIn_2S_4$-based S-scheme heterojunctions are discussed and summarized, including the utilization of advanced *in-situ* characterization techniques to further illuminate the photocatalytic mechanism, the DFT-assisted design of catalysts to increase the selectivity of products during photocatalytic CO_2 reduction, and extending the photoresponse of $ZnIn_2S_4$-based S-scheme heterojunction to near-infrared range, *etc.*

1. Introduction

The continuous growth of human demand for fossil fuels has led to energy crises and severe environmental pollution. Therefore, there is an urgent need to develop effective strategies to address these issues [1-3]. Photocatalytic technology is considered to have important application prospects in utilizing solar energy to solve energy and environmental problems [4-6]. Since Fujishiman *et al.* [7] discovered in 1972 that TiO_2 can be used as a photocatalyst to split water to generate hydrogen gas under ultraviolet light irradiation, photocatalysis technology and semiconductor photocatalyst materials have been widely applied in various areas such as CO_2 reduction [8-10], hydrogen production [11-13], and destruction of toxic and harmful pollutants [14-16].

Researchers have developed various types of photocatalysts, such as metal oxides [17-19], graphite nitride carbon ($g-C_3N_4$) [20-22], metal sulfides [23-25], metal-organic frameworks (MOFs) [26-29], covalent organic frameworks (COFs) [30-32]. Among them, $ZnIn_2S_4$ (ZIS) has received intensive attention due to its unique layered structure, suitable bandgap, excellent visible light absorption, simple and flexible preparation methods, and good chemical stability [33]. However, $ZnIn_2S_4$, as a photocatalyst, suffers photo-generated carrier recombination and photo-corrosion, which restrains its large-scale practical application [34]. Therefore, some modification strategies have been adopted to improve the photocatalytic performance of $ZnIn_2S_4$, such as morphology regulation [35-37], element doping [38-40], vacancy engineering [41-43], and construction of heterojunctions [44-46]. Among them, constructing heterojunctions can achieve spatial separation of photo-generated carriers and effectively suppress photo-corrosion [47].

As shown in Fig. 1, various types of $ZnIn_2S_4$-based heterojunctions have been developed, such as Schottky heterojunction, type-I heterojunction, type-II heterojunction, p-n heterojunction, Z-scheme heterojunction, S-scheme heterojunction, ternary and quaternary heterojunction [48]. Type-II and Z-scheme heterojunctions have received great attention and extensive exploration. For type-II heterojunctions, spatial separation of photo-generated carriers can be achieved, but it reduces the redox ability of photocatalysts and is not conducive to photocatalytic reactions. In addition, due to electrostatic repulsion, the transfer of electrons from the conduction band of one semiconductor to that of another semiconductor and the transfer of holes from the valence band of

---

* Corresponding author.
E-mail address: yfrao@mail.xjtu.edu.cn (Y. Rao).

https://doi.org/10.1016/j.cclet.2024.110108
1001-8417/

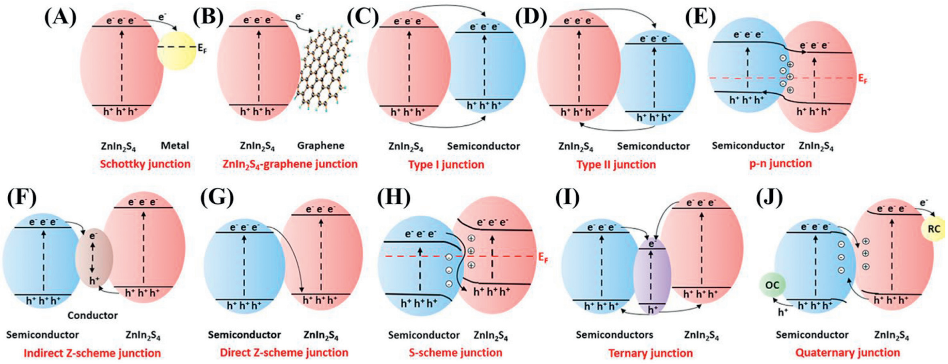

Fig. 1. Illustration of (A) Schottky junction, (B) $ZnIn_2S_4$-graphene junction, (C) type I junction, (D) type II junction, (E) p-n junction, (F) indirect Z-scheme junction, (G) direct Z-scheme junction, (H) S-scheme junction, (I) ternary junction, and (J) quaternary junction. RC and OC refer to reduction cocatalyst and oxidation cocatalyst, respectively. Copied with permission [48]. Copyright 2022, EcoMat.

one semiconductor to that of another semiconductor is difficult to achieve [49]. Z-scheme heterojunctions include indirect and direct Z-scheme heterojunctions. As shown in Fig. 1F, in the case of indirect Z-scheme heterojunction, photogenerated electrons on the conduction band of semiconductors and photogenerated holes on the valence band of $ZnIn_2S_4$ are expected to migrate to the conductor for recombination. However, photogenerated electrons on the conduction band of $ZnIn_2S_4$ and holes on the valence band of semiconductor will preferentially migrate to the conductor due to a larger potential difference between conductor and the conduction band of $ZnIn_2S_4$ than that between the conduction band of semiconductor and conductor [50]. Therefore, the proposed charge transfer pathway is incorrect and the mechanism of charge transfer remains unclear. The proposed migration direction of photogenerated carriers of direct Z-scheme heterojunctions developed from indirect Z-scheme heterojunctions also remains in debate [51]. In order to tackle the controversies in the aforementioned heterojunctions, a new concept of S-scheme heterojunction was proposed based on the direct Z-scheme heterojunction [52]. Since then, there has been a surge in studies on new S-scheme heterojunctions, and many studies on $ZnIn_2S_4$-based S-scheme heterojunctions have been reported, such as $g\text{-}C_3N_4$/ZIS [53], Bi_3TaO_7/ZIS [54], In_2O_3/ZIS [55], and TpPa-1-COF/ZIS [56]. However, S-scheme heterojunctions still have some disadvantages, including poor lattice matching, limited heterojunction contact interfaces, and small Fermi-level differences [57].

Therefore, in this review, we not only introduce the design principles and characterization methods of $ZnIn_2S_4$-based S-scheme heterojunction photocatalysts, but also the improvement strategies of $ZnIn_2S_4$-based S-scheme heterojunction photocatalysts (Fig. 2). Finally, based on current research progress, we propose the challenges and future researches focuses of $ZnIn_2S_4$-based S-scheme heterojunction.

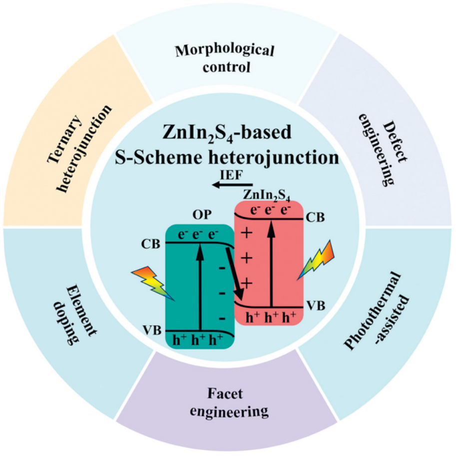

Fig. 2. The improvement methods of $ZnIn_2S_4$-based S-scheme heterojunction.

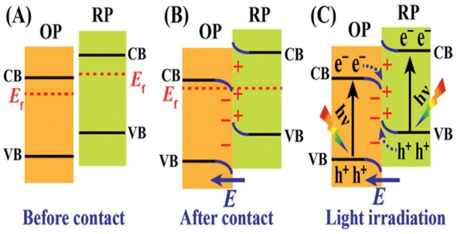

Fig. 3. Charge-transfer processes in an S-scheme heterojunction. (A) before contact, (B) after contact, (C) photogenerated charge carrier transfer process in S-scheme mode. Copied with permission [51]. Copyright 2020, Elsevier Inc.

2. ZnIn2S4-based S-scheme heterojunctions

2.1. The concept and design principles of S-scheme heterojunctions

S-scheme heterojunctions are composed of oxidation photocatalysts (OP) and reduction photocatalysts (RP) [58]. As shown in Fig. 3, RP has a smaller work function and a higher Fermi level compared to OP. When the two are in close contact, electrons in RP are spontaneously transferred to OP through the interface until the Fermi levels are the same. Therefore, at the interface, RP is positively charged due to the loss of electrons, while OP is negatively charged, thus naturally generating an internal electric field from RP to OP. Meanwhile, RP and OP exhibit upward and downward band bending at the interface, respectively. When the composite catalyst is illuminated, the electrons of RP and OP are excited from the valence band (VB) to the conduction band (CB), leaving holes in their VB, resulting in the generation of photo-generated electron-hole pairs, respectively.

The co-operation of internal electric field, band bending, and Coulombic force accelerates the recombination of photo-generated electrons in OP and photo-generated holes in RP, thereby suppressing the recombination of photo-generated electron-hole pairs in RP and OP, and retaining the powerful photo-generated electrons in the CB of RP and holes in the VB of OP [51]. Jiao *et al.* [59] selectively synthesized different types of $g\text{-}C_3N_4$ homojunctions, including CN/4ACN (type-II), CN/8PCN (S-scheme) and 4ACN/8PCN (S-scheme), by adjusting the doping amount of Ag and P. Due to the high redox potential of S-scheme homojunctions, CN/8PCN and 4ACN/8PCN exhibited HER and degradation of tetracycline (TC). In

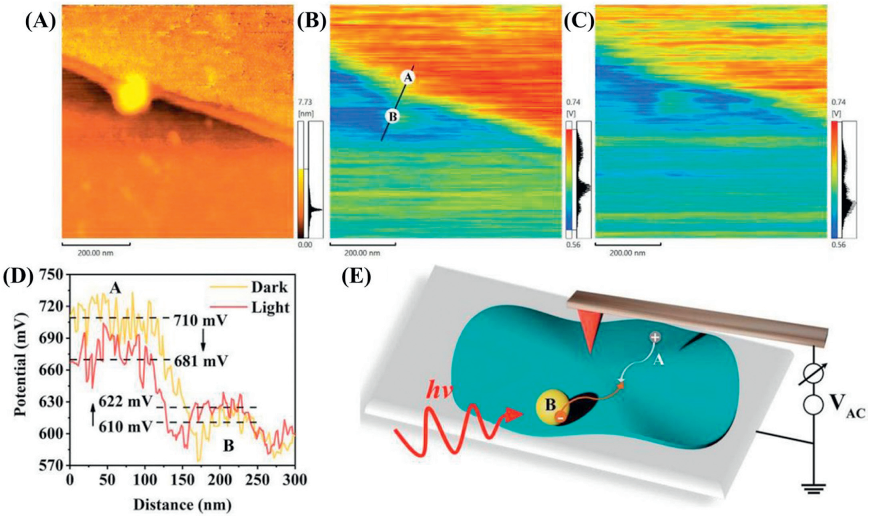

Fig. 4. (A) Atomic force microscopy image of CP composite, (B, C) corresponding surface potential distribution of CP in darkness (B) and under light irradiation (C). (D) The line-scanning surface potential from point A to B. (E) The schematic illustration of photoirradiation KPFM. Copied with permission [64]. Copyright 2021, Wiley-VCH GmbH.

addition, the hydrogen production rate of 4ACN/8CN was 2.1 times that of CN/4ACN. Therefore, the S-scheme heterojunction not only achieves charge separation but also exhibits the higher redox ability than type-II heterojunction, greatly improving photocatalytic performance.

As an n-type reduction photocatalyst, $ZnIn_2S_4$ needs to combine with another lower Fermi level oxidation photocatalyst to construct an S-scheme heterojunction in order to improve the redox ability of the composite photocatalyst [60]. In addition, $ZnIn_2S_4$ with different morphologies from 0D to 3D can be synthesized; the unique S-Zn-S-In-S-In-S layered structure of $ZnIn_2S_4$ makes its stacking structure easy to peel off and combine with another oxidation photocatalyst to construct heterojunctions [61]. Therefore, the design of $ZnIn_2S_4$-based S-scheme heterojunction photocatalysts has attracted growing interests.

2.2. Characterization methods of S-scheme heterojunctions

2.2.1. In situ irradiated X-ray photoelectron spectroscopy

The change in elemental binding energy indicates the change in electron density. The decrease in electron density after losing electrons leads to an increase in binding energy, while the increase in electron density after obtaining electrons leads to a decrease in binding energy [62]. Therefore, when RP and OP are in close contact, if an S-scheme heterojunction is successfully constructed, due to the difference in their work functions, the electrons of RP will transfer to OP until the Fermi level is the same, manifested as the binding energies of RP shifting toward higher energy levels, while the binding energies of OP moving toward lower energy levels. When illuminated, the photogenerated electrons in the OP conduction band will migrate to RP and recombine with the photogenerated holes in the RP valence band, manifested as the binding energies of RP shifting toward lower energy levels, while the binding energies of OP shifting toward higher energy levels [63]. The change in the binding energy of *in-situ* XPS suggests the transfer direction of charge carriers in heterojunctions, providing direct evidence for the successful construction of S-scheme heterojunctions.

2.2.2. Atomic force microscope (AFM)

Kelvin probe force microscopy (KPFM) is a derivative of AFM, which can scan the morphology of AFM while detecting its surface potential and can be used to evaluate the charge transfer process [13]. Yu *et al.* [64] constructed inorganic/organic heterojunctions by *in-situ* growth of CdS nanocrystals on the surface of pyrene-alt-triphenylamine (PT), and demonstrated the charge transfer mechanism of S-scheme heterojunctions between CdS/PT through KPFM, with PT serving as a reducing photocatalyst and CdS as an oxidizing photocatalyst. As shown in Fig. 4, when CdS and PT come into close contact, electrons will transfer from PT to CdS. Therefore, under dark conditions, the surface potential difference between PT (point A) and CdS (point B) is about 100 mV, indicating the formation of an internal electric field from point A to point B. When illuminated by light, the surface potential of point A decreases significantly, while the surface potential of point B increases, indicating the transfer of photo-generated electrons from CB of CdS to VB of PT. Therefore, KPFM characterization technology can also be used to characterize the charge transfer pathway in S-scheme heterojunctions.

2.2.3. Electron paramagnetic resonance (EPR)

Since the successful construction of S-scheme heterojunctions leads to the recombination of photo-generated carriers with weak redox ability, and the strong redox ability of composite photocatalysts is retained, the formation of S-scheme heterojunctions can be confirmed by EPR detection of free radicals generated during the photocatalytic process, such as hydroxyl and superoxide radicals [65]. Yu *et al.* [66] designed a heterojunction with a core-shell structure of $TiO_2@ZnIn_2S_4$ for efficient photocatalytic reduction of CO_2, and the type of heterojunction was determined through EPR test. As shown in Fig. 5A, based on the band structures of TiO_2 and $ZnIn_2S_4$, the electrons on the CB of $ZnIn_2S_4$ can reduce O_2 to $^{\bullet}O_2^-$, but the holes on the VB of $ZnIn_2S_4$ cannot oxidize H_2O to $^{\bullet}OH$; while the electrons on the CB of TiO_2 cannot reduce O_2 to $^{\bullet}O_2^-$, but the holes on the VB of TiO_2 can oxidize H_2O to $^{\bullet}OH$.

Therefore, as shown in Figs. 5B and C, the DMPO-$^{\bullet}OH$ signal and the extremely weak DMPO-$^{\bullet}O_2^-$ signal over TiO_2, as well as the DMPO-$^{\bullet}O_2^-$ signal over $ZnIn_2S_4$, can be observed in the EPR spectra, while the DMPO-$^{\bullet}OH$ signal over $ZnIn_2S_4$ cannot be detected. In the case of $TiO_2@ZnIn_2S_4$, the intensity of DMPO-$^{\bullet}OH$ and DMPO-$^{\bullet}O_2^-$ signals is stronger than that over the sole-TiO_2 and sole-$ZnIn_2S_4$, respectively. If $TiO_2@ZnIn_2S_4$ is a type-II heterojunction as shown in Fig. 5D, both $^{\bullet}OH$ and $^{\bullet}O_2^-$ cannot be generated. Therefore, as shown in Fig. 5E, $TiO_2@ZnIn_2S_4$ is an S-scheme heterojunction, retaining strong oxidation and reduction capability of both, resulting in the production of both $^{\bullet}OH$ and $^{\bullet}O_2^-$.

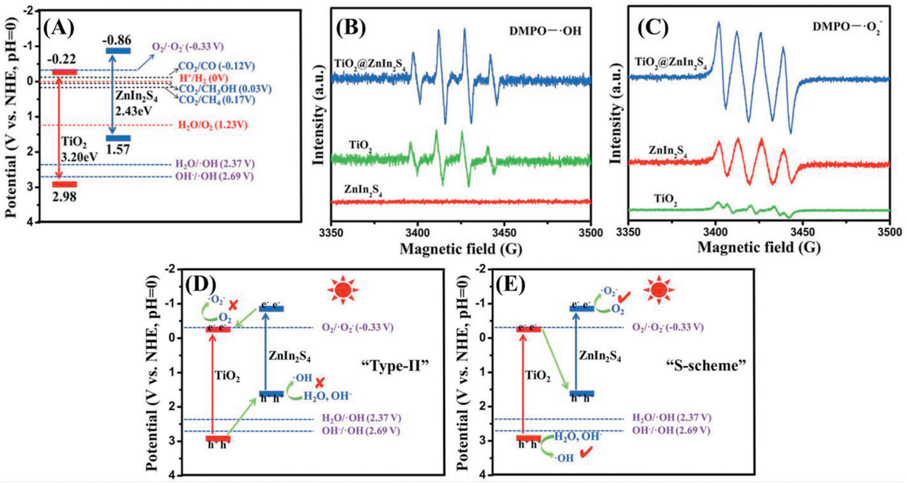

Fig. 5. (A) Band structures of samples. Electron paramagnetic resonance (EPR) spectra of (B) DMPO-$\cdot$OH adducts (in aqueous solution) and (C) DMPO-$\cdot O_2^-$ adducts (in methanol solution) over TiO_2, $ZnIn_2S_4$, and $TiO_2@ZnIn_2S_4$ under illumination for 2 min. Schematic diagrams of (D) conventional type-II and (E) S-scheme heterojunction. Reproduced with permission [66]. Copyright 2021, Wiley-VCH GmbH.

3. Improvement strategies for $ZnIn_2S_4$-based S-scheme heterojunction

Efficient photocatalytic performance can be achieved by reasonably designing S-scheme heterojunctions with fast interface charge transfer and high redox potential [67]. However, S-scheme heterojunctions are usually composed of two n-type semiconductors, and the Fermi energy level difference between the two components is small, resulting in weak electric field driving force for interfacial charge transfer, low charge separation efficiency, and thus, poor photocatalytic performance [68]. Therefore, some modification strategies, such as morphological control, defect engineering, element doping, have been applied to provide S-scheme heterojunctions with more active sites and band arrangements with larger interface potential differences, thereby promoting charge separation and improving activity. The improvement strategies of $ZnIn_2S_4$-based S-scheme heterojunction are summarized in Table 1.

3.1. Morphological control

By reasonable morphological design, photocatalytic activity of S-scheme heterojunction can be greatly improved [69]. Dai *et al.* [70] synthesized the S-scheme heterojunction $CdLa_2S_4/ZnIn_2S_4$ by loading fishbone-like $CdLa_2S_4$ on micrometer flower-shaped ZIS based on different work functions. The unique structure provided a large contact area between the catalyst and the reaction solution. Through careful design of the morphology and the construction of S-scheme heterojunction, the degradation efficiency of sulfamethoxazole was as high as 98.9%.

However, the 2D sheet-like structure of $ZnIn_2S_4$ often undergoes excessive self-assembly to produce flower-shaped microspheres, which greatly reduces the active sites and leads to photogenerated carrier recombination [71]. Therefore, constructing heterojunctions between catalysts with appropriate morphology and ZIS nanosheets can prevent aggregation and improve photocatalytic activity [72]. Zhao *et al.* [73] constructed the S-scheme heterojunction ZIS/WO_3 by *in-situ* growth of 2D ZIS nanosheets on 1D WO_3 nanorods. The 1D nanorod structure can avoid the aggregation of ZIS sheet-like structures and has a large specific surface area and a short charge transfer path. The vertical distribution of 2D nanosheets on the surface of 1D nanorods can improve the surface activity and light absorption of photocatalysts. Thanks to the S-scheme heterojunction and exquisite morphology design, the ZIS/WO_3 heterojunction exhibited excellent photocatalytic activity, with a hydrogen production rate of 300 μmol g^{-1} h^{-1}.

Compared to 1D/2D composite, 2D/2D composite not only prevents the aggregation of ZIS nanosheets, but also the OP substrate of 2D can provide a larger specific surface area and tighter surface contact, thereby providing more adsorption and active sites and rich charge transfer channels for the construction of S-scheme heterojunctions [74]. Wang *et al.* [75] prepared mossy tile-like morphology S-scheme heterojunction ZIS/CMS by *in-situ* growth of ZIS nanosheets on Cu_2MoS_4 plates. The unique structure inhibited the aggregation of ZIS nanosheets, provided more active sites, and led to the formation of a tight interface S-scheme heterojunction between ZIS and CMS. The photocatalytic hydrogen production rate of ZIS/CMS was as high as 1298 μmol g^{-1} h^{-1} and had excellent stability. In addition, due to the unique layered crystal structure of $Bi_4Ti_3O_{12}$, Zhou *et al.* [76] prepared an S-scheme heterojunction 2D/2D $ZnIn_2S_4/Bi_4Ti_3O_{12}$ using molten salt method and low-temperature solvothermal method. Benefiting from the abundant active sites, tight contact interfaces, and effective separation of photo-generated carriers, ZIS/BTO exhibited good tetracycline removal efficiency, with a rate constant of 0.023 min^{-1}.

Compared to other morphology engineering, hollow structures can offer nanomaterials some unique advantages including large specific surface area, a great number of active sites, and improved light utilization through multiple reflections and scattering of light [77]. Li *et al.* [78] prepared an S-scheme heterojunction ZIS/HCNT with core-shell structure by *in-situ* growth of ZIS nanosheets on g-C_3N_4 hollow nanotubes. Compared to 1D nanorods, 1D nanotubes had higher light utilization efficiency and stronger charge transfer ability due to multiple reflection effects and thin tube walls. *In situ* growth promoted the formation of a uniform and tight interface between the two, and simultaneously utilized the advantages of hollow structure and S-scheme heterojunction, exhibiting a high CO yield of 883 μmol g^{-1} h^{-1}.

3.2. Defect engineering

For S-scheme heterojunctions, increasing the difference in work function between RP and OP can also enhance the strength of the internal electric field, thereby promoting the transfer of interfacial charges in heterojunctions and the separation of photo-generated carriers in photocatalysts [79]. The introduction of vacancies can regulate the work function of catalysts, thus improving S-scheme

Table 1
Summary table of the improvement methods of $ZnIn_2S_4$-based S-scheme heterojunction.

Improvement methods	Photocatalyst	Light source	Application	Performance	Ref.
Morphological control	0D Bi_3TiO_7 nanodots/3D $ZnIn_2S_4$ nanoflowers	300 W Xe lamp ($\lambda > 420$ nm)	H_2 evolution	13.7 μmol g^{-1} h^{-1}	[54]
	1D TiO_2 nanofiber/2D $ZnIn_2S_4$ nanosheets	300 W Xe lamp	H_2 evolution	6.03 mmol g^{-1} h^{-1}	[45]
	1D WO_3 nanorods/2D $ZnIn_2S_4$ nanosheets	300 W Xe lamp ($\lambda > 400$ nm)	H_2 evolution	300 μmol g^{-1} h^{-1}	[73]
	2D fishbone-like $CdLa_2S_4$/3D $ZnIn_2S_4$ nanoflowers	300 W Xe lamp	H_2 evolution	1582.3 μmol g^{-1} h^{-1}	[70]
	1D hexagonal g-C_3N_4 tubes/2D $ZnIn_2S_4$ nanosheets	300 W Xe lamp	CO_2 reduction	883 μmol g^{-1} h^{-1} CO	[78]
	0D ZnO nanoparticles/3D $ZnIn_2S_4$ nanoflowers	300 W Xe lamp	H_2 evolution	13.64 mmol g^{-1} h^{-1}	[62]
	1D ZnO nanorods@2D $ZnIn_2S_4$ nanosheets	300 W Xe lamp	CO_2 reduction	39.76 μmol g^{-1} h^{-1} CO 3.92 μmol g^{-1} h^{-1} CH_4	[10]
	1D WO_3 nanofiber@2D $ZnIn_2S_4$ nanosheets	300 W Xe lamp	H_2 evolution	8500 μmol g^{-1} h^{-1}	[46]
	2D sheet-like $Bi_4Ti_3O_{12}$/2D $ZnIn_2S_4$ nanosheets	300 W Xe lamp ($\lambda > 420$ nm)	Tetracycline degradation	$K = 0.02234$ min^{-1}	[76]
	Mossy tile-like 2D/2D Cu_2MoS_4/$ZnIn_2S_4$	300 W Xe lamp ($\lambda > 400$ nm)	H_2 evolution	1298 μmol g^{-1} h^{-1}	[75]
	$ZnIn_2S_4$ nanoflake/24-faceted concave MIL-88(Fe)	300 W Xe lamp ($\lambda > 420$ nm)	Tetracycline degradation	$K = 0.02663$ min^{-1}	[44]
	3D TiO_2 hollow spheres@2D $ZnIn_2S_4$ nanosheets	300 W Xe lamp	CO_2 reduction	9.28 μmol g^{-1} h^{-1} CO 4.26 μmol g^{-1} h^{-1} CH_4 4.78 μmol g^{-1} h^{-1} CH_3OH	[66]
	1D Ta_2O_5 nanofiber/2D $ZnIn_2S_4$ nanosheets	300 W Xe lamp ($\lambda > 400$ nm)	CO_2 reduction	101.62 μmol g^{-1} h^{-1} CO 7.22 μmol g^{-1} h^{-1} CH_4	[25]
	1D hollow corncob-like $LaFeO_3$/2D $ZnIn_2S_4$ nanosheets	300 W Xe lamp ($\lambda > 420$ nm)	H_2 evolution	1.85 mmol g^{-1} h^{-1}	[67]
	1D TiO_2 nanotube/3D $ZnIn_2S_4$ nanoflower	Xe lamp solar simulator	RhB degradation	$K = 0.03253$ min^{-1}	[19]
Defect engineering	Sv-$ZnIn_2S_4$/g-C_3N_4	300 W Xe lamp ($\lambda > 420$ nm)	Tetracycline degradation	$K = 0.03361$ min^{-1}	[83]
	Sv-ZnS/$ZnIn_2S_4$	300 W Xe lamp ($\lambda > 420$ nm)	H_2 evolution	2912.3 μmol g^{-1} h^{-1}	[81]
Element doping	Mo-ZIS@$NiTiO_3$	300 W Xe lamp ($\lambda > 420$ nm)	H_2 evolution	14.06 mmol g^{-1} h^{-1}	[84]
	MoO_3@Mo-ZIS	300 W Xe lamp ($\lambda > 420$ nm)	H_2 evolution	5.5 mmol g^{-1} h^{-1}	[85]
Facet engineering	$ZnIn_2S_4$/BiOBr-(001)	300 W Xe lamp ($320 < \lambda < 780$ nm)	H_2 evolution	17 mmol g^{-1} h^{-1}	[86]
Photothermal-assisted photocatalytic	FeS_2@$ZnIn_2S_4$	300 W Xe lamp	H_2 evolution	5.05 mmol g^{-1} h^{-1}	[87]
	Co_3O_4@$ZnIn_2S_4$	300 W Xe lamp	H_2 evolution	18.9 mmol g^{-1} h^{-1}	[88]
	MoO_{3-x}@$ZnIn_2S_4$	300 W Xe lamp	CO_2 reduction	4.65 μmol g^{-1} h^{-1} CO 28.3 μmol g^{-1} h^{-1} CH_4	[89]
	$Cu_{2\text{-}x}S$@$ZnIn_2S_4$	300 W Xe lamp	H_2 evolution	4653.43 μmol g^{-1} h^{-1}	[90]
	g-C_3N_4@$ZnIn_2S_4$	300 W Xe lamp	H_2 evolution	4075.65 μmol g^{-1} h^{-1}	[91]
Ternary heterojunction	CNQDs/TCN/$ZnIn_2S_4$	300 W Xe lamp ($\lambda>420$ nm)	Petroleum hydrocarbon degradation	$K = 0.4362$ g L^{-1} h^{-1}	[92]
	g-C_3N_4/TiO_2/$ZnIn_2S_4$ graphene aerogel	300 W Xe lamp	H_2 evolution	6531.9 μmol g^{-1} h^{-1}	[93]
	BN/MXene/$ZnIn_2S_4$	300 W Xe lamp	H_2 evolution	1455 μmol g^{-1} h^{-1}	[15]
	α-Fe_2O_3@$ZnIn_2S_4$/Ti_3C_2	500 W Xe lamp ($\lambda>420$ nm)	Bisphenol A degradation	$K = 0.02595$ min^{-1}	[69]

heterojunctions through defect engineering [80]. Liu *et al.* [81] first prepared ZIF-8/ZIS with atomic level tight interfaces through the ZIS self-sacrificing reaction mechanism and then controlled the *in-situ* sulfurization time to convert ZIF-8/ZIS into an S-scheme heterojunction S_v-ZnS/ZIS with controllable sulfur vacancy concentration. The introduction of sulfur vacancies changed the work function of ZnS, increasing the difference in work function between ZIS and ZnS from 1.41 eV to 1.53 eV. S_v-ZnS/ZIS with enhanced internal electric field strength and tight interface exhibited excellent photocatalytic hydrogen production performance; the hydrogen production rate of S_v-ZnS/ZIS was 2912.3 ± 185.9 μmol g^{-1} h^{-1}, which was much higher than the hydrogen production rate of other ZnS/ZIS photocatalyst by 103 μmol g^{-1} h^{-1} [82].

The bridging of interface chemical bonds can provide a charge transmission channel, which is conducive to faster electron transfer between interfaces and further expands the advantages provided by defect engineering [94]. Sun *et al.* [83] combined g-C_3N_4 with ZIS with sulfur vacancies to construct an S-scheme heterojunction S_v-ZIS/CN with efficient degradation of tetracycline. Within 90 min, the tetracycline degradation rate of S_v-ZIS/CN reached

96.36%, much higher than the 64.62% tetracycline degradation rate of ZIS-S/CN prepared by mechanical stirring. The excellent activity was attributed to the introduction of sulfur vacancies, the formation of interface S-C bonds, and the internal electric field, which jointly promoted charge transfer in S-scheme heterojunctions and significantly improved the separation efficiency of photo-generated carriers.

3.3. Element doping

The combination of S-scheme heterojunction and element doping can synergistically improve light absorption and promote the separation of photo-generated carriers, thereby enhancing photocatalytic performance. Su *et al.* [85] utilized the thermal solubility of MoO_3 to obtain uniform *in-situ* Mo doped ZIS wrapped MoO_3 S-scheme heterojunction. *In situ* Mo doping not only improved light absorption, but also led to the formation of Mo-S bonds, reducing the ΔG_{H^*}, leading to excellent photocatalytic hydrogen production performance (5.5 mmol g^{-1} h^{-1}), which was much better than that of MoO_3@ZIS (2.4 mmol g^{-1} h^{-1}).

Element doping can achieve a larger Fermi energy level difference between heterojunctions by adjusting the work function, resulting in a stronger internal electric field and higher interfacial charge transfer efficiency [95]. In addition, elemental doping can also change the hydrophilicity of the catalyst surface, promoting the adsorption and activation of H_2O molecules [96]. Zhu *et al.* [84] constructed an S-scheme heterojunction by *in-situ* growth of Mo-modified $ZnIn_2S_4$ nanosheets on rod-shaped $NiTiO_3$ using the hydrothermal method (Mo-ZIS@NTO). Mo doping significantly increased the Fermi level of ZIS, resulting in an increase in the Fermi level difference between ZIS and NTO from 1.0 eV to 1.43 eV. The enhanced internal electric field as a powerful driving force can promote the separation and transmission of photo-generated charge carriers. The increased hydrophilicity of Mo-ZIS helped to adsorb more water molecules for photocatalytic reduction of hydrogen production. Through the combined effect of S-scheme heterojunction and Mo doping, Mo-ZIS@NTO exhibited excellent performance, with a hydrogen production rate of 14.06 mmol g^{-1} h^{-1} under visible light, which was 2.2 times higher than ZIS@NTO.

3.4. Facet engineering

For S-scheme heterojunction structures, the transfer and spatial separation of photo-generated carriers in RP and OP occur between interfaces. Different crystal planes of the same crystal phase will have different energy band levels due to differences in their surface electronic structures [97]. Therefore, the interface contact between ZIS and other semiconductors with different facet exposure can lead to heterojunctions with different band structures, thereby affecting the migration of photo-generated carriers between interfaces [98]. Xi *et al.* [86] used crystal plane engineering to adjust the arrangement of energy bands, regulate charge transfer and separation between interfaces, and significantly improved the photocatalytic activity of S-scheme heterojunctions for hydrogen production. ZIS/BOB-(010) and ZIS/BOB-(001) S-scheme heterojunctions were prepared by growing ZIS nanosheets on BiOBr nanoparticles mainly composed of (010) and (001) facet, respectively. The Fermi energy level difference (0.70 eV) between BOB-(001) and ZIS was larger than that (0.49 eV) between BOB-(010) and ZIS. Due to the larger Fermi energy level difference between BOB-(001) and ZIS, the interface exhibited more significant band bending and stronger internal electric field, accelerating the transfer efficiency of photo-generated carriers through the BOB-(001)/ZIS interface, thereby promoting the recombination of useless photo generated carriers with weak redox ability and the spatial separation of useful photo-generated electron-hole pairs with strong redox ability. Therefore, BOB-(001)/ZIS exhibited excellent photocatalytic hydrogen production efficiency, up to 17.0 mmol g^{-1} h^{-1}, which was 4.0 and 2.4 times higher than that over ZIS and BOB-(010)/ZIS, respectively.

3.5. Photothermal-assisted photocatalysis

As a temperature sensitive photocatalyst, the increase in temperature leads to an increase in its activity of $ZnIn_2S_4$ [88]. Therefore, coupling $ZnIn_2S_4$ nanosheets with photothermal materials to construct an S-scheme heterojunction can achieve higher photocatalytic activity, which is beneficial for the development of photothermal-assisted photocatalytic systems [91]. Chen *et al.* [87] constructed an S-scheme heterojunction by *in-situ* growth of ZIS nanosheets on FeS_2 hollow spheres, a photothermal material. The photothermal effect of FeS_2 increased the temperature of the reaction system and accelerated charge transfer; the surface ZIS coating could effectively prevent heat loss. Under simulated solar radiation, the hydrogen production rate over FS_2@ZIS was as high as 5.05 mmol g^{-1} h^{-1}, which was 47.9 and 53.7 times that over the original ZIS and FeS_2, respectively.

In recent years, the localized surface plasmon resonance (LSPR) effect has also been found in some non-stoichiometric compounds, enabling them to possess the ability of photothermal synergistic catalytic reactions [90]. Xiong *et al.* [89] successfully synthesized the S-scheme heterojunction MoO_{3-x}@ZIS by *in-situ* growth of ZIS nanosheets on 1D needle-like MoO_{3-x}. Due to the large number of oxygen vacancies in MoO_{3-x}, Mo^{6+} was reduced to Mo^{5+}, resulting in an increase in free electron concentration and the LSPR effect. Under the synergistic effect of S-scheme heterojunction and photothermal conversion, the reaction efficiency and CH_4 selectivity of CO_2 reduction were improved. Under full spectrum irradiation, the yields of CO and CH_4 over MoO_{3-x}@ZIS reached 4.65 and 28.3 µmol g^{-1} h^{-1}, respectively, and CH_4 selectivity was as high as 85.89%, with CH_4 yield, 19.4 and 11.7 times higher than that over MoO_{3-x} and ZIS.

3.6. Ternary heterojunction

Compared to binary S-scheme heterojunctions with single-channel charge transfer, charge transfer of multicomponent heterojunctions with multi-carrier transport paths is more efficient [99]. Bai *et al.* [100] anchored the S-scheme heterojunction ZIS-$NiSe_2$ onto Ti_3C_2 MXene using a two-step solvothermal method. Due to the higher Fermi level of ZIS compared to $NiSe_2$ and Ti_3C_2 MXene, the charge of ZIS will be transferred to $NiSe_2$ and Ti_3C_2 MXene. When the Fermi levels of the three were balanced, an internal electric field was generated between the interface of ZIS and $NiSe_2$, and a Schottky barrier was formed between the interface of ZIS and Ti_3C_2 MXene. When illuminated, the photo-generated electrons in Ti_3C_2 CB will recombine with the photo-generated holes in ZIS VB in the internal electric field, while the photo-generated electrons on ZIS CB will migrate along the Schottky junction to Ti_3C_2 MXene, thereby suppressing the photo-generated electron reflux in ZIS. Under the synergistic effect of Schottky junction and S-scheme heterojunction, the dual charge transfer pathways in ZIS can achieve rapid photo-generated carrier separation; Ti_3C_2-ZIS-$NiSe_2$ exhibited a hydrogen production rate of 23.51 mmol g^{-1} h^{-1} under visible light, which was 23.51, 8.31, and 3.54 times higher than that over ZIS, Ti_3C_2-ZIS, and ZIS-$NiSe_2$, respectively.

Xia *et al.* [92] promoted the charge transfer of 2D/2D S-scheme heterojunctions without close contact region by inserting 0D CN-QDs between 2D/2D TCN (tubular g-C_3N_4)/ZIS S-scheme heterojunctions to construct Schottky junctions. The synergistic effect of this Schottky junction and S-scheme heterojunction greatly improved the transfer and separation of charges between the 2D/2D

TCN/ZIS interfaces, generating abundant $^{\bullet}OH$, $^{\bullet}O_2^-$ and photo-generated holes to remove carbon atoms in $C_{14}H_{30}$ one by one, ultimately efficiently degrading n-tetradecane into CO_2 and H_2O.

Most studies on S-scheme photocatalysts have focused on binary composite materials. However, there is still considerable potential for improvement in charge transfer, quantum efficiency, and light capture ability of the binary S-scheme photocatalyst [101]. The dual S-scheme heterojunction can further optimize the photo-generated charge transfer pathway, and its excellent photocatalytic activity can be attributed to the synergistic effect between the three components [102]. Liu *et al.* [93] used the isoelectric point assisted calcination method to fix g-C_3N_4, TiO_2, and ZIS on the graphene aerogel carrier and constructed a dual S-scheme heterojunction g-C_3N_4/TiO_2/ZIS (CTZA) which efficiently degraded methyl orange (MO) under visible light irradiation. Due to the lower Fermi level of TiO_2 compared to g-C_3N_4 and ZIS, when the three came into contact, the charges on g-C_3N_4 and ZIS will transfer to TiO_2 until the Fermi level was balanced, and a dual internal electric field directed by g-C_3N_4 and ZIS towards TiO_2 was formed. Under illumination, the photo-generated electrons in the CB of TiO_2 recombined with the photo-generated holes in g-C_3N_4 and ZIS, thereby retaining the holes with strong oxidation ability in the VB of TiO_2 and the electrons with strong reduction ability in g-C_3N_4 and ZIS. Graphene with excellent conductivity can further promote the transfer and separation of photo-generated charge carriers, resulting in a degradation rate of 97.5% for MO over CTZA within 30 min, much higher than that over ZIS, TiO_2 and g-C_3N_4.

4. Conclusions and prospects

$ZnIn_2S_4$, as a reducing ternary metal sulfide photocatalyst, has received widespread attention due to its narrow bandgap and visible-light-responsive properties. Unfortunately, the rapid recombination of photo-generated carriers and photo-corrosion of $ZnIn_2S_4$ curbs its practical application. Although constructing S-scheme heterojunctions by combining with other semiconductor materials can improve the photocatalytic activity of $ZnIn_2S_4$, developing effective strategies which can further improve the photocatalytic performance of $ZnIn_2S_4$-based S-scheme heterojunctions still remain a challenge. This article introduces the concept and design principles of $ZnIn_2S_4$-based S-scheme heterojunction, and summarizes its current improvement strategies for S-scheme heterojunction, including morphology control, defect engineering, element doping, facet engineering, photothermal assisted catalysis, and ternary heterojunction. Although the studies on the improvement of $ZnIn_2S_4$-based S-scheme heterojunctions have made significant progress, a few research areas can be focused in the future.

Firstly, to identify the direction of charge transfer in S-scheme heterojunctions more accurately, more advanced *in-situ* characterization techniques should be applied to demonstrate the charge transfer process besides *in-situ* XPS and AFM. For instance, time-resolved photoemission electron microscopy (TR-PEEM) can be applied to visually showcase the transfer of electrons and holes of $ZnIn_2S_4$-based S-scheme heterojunctions.

Secondly, combining experiments with theoretical simulation calculations helps understand the dynamics of charge carrier transfer and identify the active sites of OP and RP, which benefits the rational design of photocatalysts for the selective reaction. For example, for photocatalytic reduction of CO_2 using $ZnIn_2S_4$-based S-scheme heterojunctions, active sites favorable for the generation of reaction intermediates can be predicted through theoretical calculations, and the electron enrichment ability of reducing sites can be increased by improving the S-scheme heterojunction. Therefore, rational design of S-scheme heterojunctions can further enhance product selectivity and generate more valuable hydrocarbon fuels.

Thirdly, previous studies focused on the improvement of $ZnIn_2S_4$-based S-scheme heterojunctions through anionic vacancies and metal doping. Cation vacancies, non-metal doping and double doping can also be applied to improve the performance of S-scheme heterojunctions in the future.

Finally, extending the photo-response of $ZnIn_2S_4$-based S-scheme heterojunction to near-infrared range through narrowing the bandgap and combining $ZnIn_2S_4$-based S-scheme heterojunction with up-conversion materials, photothermal-conversion materials or photosensitive materials can also be a research focus since near-infrared light accounts for 52% of solar light.

Declaration of competing interest

The authors declare that they have no known competing financial interests or personal relationships that could have appeared to influence the work reported in this paper.

CRediT authorship contribution statement

Hongrui Zhang: Writing – original draft. **Miaoying Cui:** Investigation. **Yongjie Lv:** Investigation. **Yongfang Rao:** Writing – review & editing. **Yu Huang:** Resources.

Acknowledgments

We are grateful to the Strategic Priority Research Program of the Chinese Academy of Sciences, China (Nos. XDA23010300 and XDA23010000) and the National Natural Science Foundation of China (Nos. 51878644 and 41573138).

References

[1] Y. Kumar, R. Kumar, P. Raizada, et al., J. Mater. Sci. Technol. 87 (2021) 234–257.
[2] W.J. Liu, H. Jiang, H.Q. Yu, Energy Environ. Sci. 12 (2019) 1751–1779.
[3] H.J. Huang, M.M. Yan, C.Z. Yang, et al., Adv. Mater. 31 (2019) 1903415.
[4] Q. Guo, C.Y. Zhou, Z.B. Ma, et al., Adv. Mater. 31 (2019) 1901997.
[5] F. Chen, H.W. Huang, L. Guo, et al., Angew. Chem. Int. Ed. 58 (2019) 10061–10073.
[6] Y. Cai, F.X. Luo, Y.J. Guo, et al., Molecules 28 (2023) 2142.
[7] A. Fujishima, K. Honda, Nature 238 (1972) 37–38.
[8] X.J. Shi, Y. Huang, Y.N. Bo, et al., Angew. Chem. Int. Ed. 61 (2022) e202203063.
[9] H. Li, C.K. Cheng, Z.J. Yang, et al., Nat. Commun. 13 (2022) 6466.
[10] Y.N. Zhang, M.Y. Xu, W.Q. Zhou, et al., J. Colloid Interf. Sci. 650 (2023) 1762–1772.
[11] X.J. Chen, J. Wang, Y.Q. Chai, et al., Adv. Mater. 33 (2021) 2007479.
[12] M.L. Xu, M. Lu, G.Y. Qin, et al., Angew. Chem. Int. Ed. 61 (2022) e202210700.
[13] B.Q. Xia, B.W. He, J.J. Zhang, et al., Adv. Energy Mater. 12 (2022) 2201449.
[14] X.Y. Chen, X. Peng, L.B. Jiang, et al., Chem. Eng. J. 427 (2022) 130945.
[15] M. Dai, Z.L. He, W.R. Cao, et al., Sep. Purif. Technol. 309 (2023) 123004.
[16] Y. Wang, X. Wu, J.Q. Liu, et al., J. Environ. Chem. Eng. 10 (2022) 107091.
[17] Y. Yuan, R.T. Guo, L.F. Hong, et al., Mater. Today Energy 21 (2021) 100829.
[18] X. Li, H.P. Jiang, C.C. Ma, et al., Appl. Catal. B: Environ. 283 (2021) 119638.
[19] E.S. Ghalehsefid, Z.G. Jahani, A. Aliabadi, et al., J. Environ. Chem. Eng. 11 (2023) 110160.
[20] B.C. Zhu, B. Cheng, J.J. Fan, et al., Small Struct. 2 (2021) 2100086.
[21] Y.F. Huang, D. Wei, Z.Y. Li, et al., J. Energy Chem. 83 (2023) 423–432.
[22] X.H. Wu, X.F. Wang, F.Z. Wang, et al., Appl. Catal. B: Environ. 247 (2019) 70–77.
[23] G.X. Zhang, Z.J. Guan, J.J. Yang, et al., Sol. RRL 6 (2022) 2200587.
[24] J. Jiang, G.H. Wang, Y.C. Shao, et al., Chin. J. Catal. 43 (2022) 329–338.
[25] K. Wang, X.L. Shao, Q. Cheng, et al., Sol. RRL 6 (2022) 2200736.
[26] N.Y. Huang, J.Q. Shen, X.W. Zhang, et al., J. Am. Chem. Soc. 144 (2022) 8676–8682.
[27] K. Sun, Y.Y. Qian, H.L. Jiang, Angew. Chem. Int. Ed. 62 (2023) e202217565.
[28] Y.P. Zhang, J.X. Xu, J. Zhou, et al., Chin. J. Catal. 43 (2022) 971–1000.
[29] R.N. Ali, W.A. Qureshi, H. Naz, et al., New J. Chem. 47 (2023) 15534–15542.
[30] R.F. Chen, Y. Wang, Y. Ma, et al., Nat. Commun. 12 (2021) 1354.
[31] J.H. Ding, X.Y. Guan, J. Lv, et al., J. Am. Chem. Soc. 145 (2023) 3248–3254.
[32] L. Sun, L.L. Li, J. Yang, et al., Chin. J. Catal. 43 (2022) 350–358.
[33] Y.J. Ren, J.J. Foo, D.Q. Zeng, et al., Small Struct. 3 (2022) 2200017.
[34] T.X. Zhang, T. Wang, F.L. Meng, et al., J. Mater. Chem. C 10 (2022) 5400–5424.
[35] X.L. Gou, F.Y. Cheng, Y.H. Shi, et al., J. Am. Chem. Soc. 128 (2006) 7222–7229.
[36] M.S. Yu, X.Y. Lv, A.M. Idris, et al., J. Colloid Interf. Sci. 612 (2022) 782–791.
[37] S.P. Ding, X.F. Liu, Y.Q. Shi, et al., ACS Appl. Mater. Interfaces 10 (2018) 17911–17922.

[38] B. Pan, Y. Wu, B. Rhimi, et al., J. Energy Chem. 57 (2021) 1–9.
[39] D.X. Zhou, X.D. Xue, X. Wang, et al., Appl. Catal. B: Environ. 310 (2022) 121337.
[40] S.Q. Zhang, Z.F. Zhang, Y.M. Si, et al., ACS Nano 15 (2021) 15238–15248.
[41] Y.Q. He, C.L. Chen, Y.X. Liu, et al., Nano Lett. 22 (2022) 4970–4978.
[42] Y.Q. He, H. Rao, K.P. Song, et al., Adv. Funct. Mater. 29 (2019) 1905153.
[43] J.W. Pan, G.X. Zhang, Z.J. Guan, et al., J. Energy Chem. 58 (2021) 408–414.
[44] Q.L. Huang, J.Q. Hu, Y.F. Hu, et al., Environ. Sci. Nano 9 (2022) 4433–4444.
[45] J.M. Li, C.C. Wu, J. Li, et al., Chin. J. Catal. 43 (2022) 339–349.
[46] S. Cao, J.G. Yu, S. Wageh, et al., J. Mater. Chem. A 10 (2022) 17174–17184.
[47] Q.H. Zhu, Q. Xu, M.M. Du, et al., Adv. Mater. 34 (2022) 2202929.
[48] V.B.Y. Oh, S.F. Ng, W.J. Ong, Ecomat 4 (2022) e12204.
[49] L.Y. Zhang, J.J. Zhang, H.G. Yu, et al., Adv. Mater. 34 (2022) 2107668.
[50] S. Wageh, A.A. Al-Ghamdi, R. Jafer, et al., Chin. J. Catal. 42 (2021) 667–669.
[51] Q.L. Xu, L.Y. Zhang, B. Cheng, et al., Chem 6 (2020) 1543–1559.
[52] J.W. Fu, Q.L. Xu, J.X. Low, et al., Appl. Catal. B: Environ. 243 (2019) 556–565.
[53] Y.N. Zhang, M. Gao, S.T. Chen, et al., Acta Phys. Chim. Sin. 39 (2023) 2211051.
[54] K. Wang, X.L. Shao, K.J. Zhang, et al., Appl. Surf. Sci. 596 (2022) 153444.
[55] L. Zhao, B.X. Yang, G.X. Zhuang, et al., Small 18 (2022) 2201668.
[56] P.Y. Dong, T. Cheng, J.L. Zhang, et al., ACS Appl. Energy Mater. 6 (2023) 1103–1115.
[57] A. Kumar, A. Khosla, S.K. Sharma, et al., Fuel 333 (2023) 126267.
[58] Q.L. Xu, S. Wageh, A.A. Al-Ghamdi, et al., J. Mater. Sci. Technol. 124 (2022) 171–173.
[59] J.J. Jiao, Z.X. Wang, J. Wang, et al., Appl. Surf. Sci. 639 (2023) 158260.
[60] Z.F. Yang, L.L. Wang, M. Fang, et al., Sep. Purif. Technol. 305 (2023) 122509.
[61] J. Wang, S.J. Sun, R. Zhou, et al., J. Mater. Sci. Technol. 78 (2021) 1–19.
[62] Z.Y. Xie, L.J. Xie, F.F. Qi, et al., J. Colloid Interf. Sci. 650 (2023) 784–797.
[63] J.J. Zhang, L.Y. Zhang, W. Wang, et al., J. Phys. Chem. Lett. 13 (2022) 8462–8469.
[64] C. Cheng, B.W. He, J.J. Fan, et al., Adv. Mater. 33 (2021) 2100317.
[65] X.N. Wang, M. Sayed, O. Ruzimuradov, et al., Appl. Mater. Today 29 (2022) 101609.
[66] L.B. Wang, B. Cheng, L.Y. Zhang, et al., Small 17 (2021) 2103447.
[67] X.L. Su, S.K. Wang, J.C. Liu, et al., Chemosphere 340 (2023) 139777.
[68] J.Q. Liu, J. Wan, L. Liu, et al., Chem. Eng. J. 430 (2022) 133125.
[69] S. Wang, X. Du, C.H. Yao, et al., Nano Res. 16 (2023) 2152–2162.
[70] M. Dai, H.J. Yu, W.H. Chen, et al., Chem. Eng. J. 470 (2023) 144240.
[71] J.J. Peng, J.Y. Yang, B. Chen, et al., Biosens. Bioelectron. 175 (2021) 112873.
[72] H.T. Fan, Z. Wu, K.C. Liu, et al., Chem. Eng. J. 433 (2022) 134474.
[73] M.Y. Zhao, S. Liu, D.M. Chen, et al., Chin. J. Catal. 43 (2022) 2615–2624.
[74] Z.T. He, C. Qian, D.M. Chen, et al., J. Colloid Interf. Sci. 651 (2023) 138–148.
[75] S.K. Wang, D.F. Zhang, P. Su, et al., J. Colloid Interf. Sci. 650 (2023) 825–835.
[76] Q. Zhou, L.H. Zhang, L.F. Zhang, et al., J. Hazard. Mater. 438 (2022) 129438.
[77] Y.C. Guo, J.M. Sun, Y. Tang, et al., Energy Environ. Sci. 16 (2023) 3462–3473.
[78] L.L. Li, D.K. Ma, Q.L. Xu, et al., Chem. Eng. J. 437 (2022) 135153.
[79] Y.X. Tan, Z.M. Chai, B.H. Wang, et al., ACS Catal. 11 (2021) 2492–2503.
[80] Z.J. Zhang, X.S. Wang, D.B. Li, et al., Small 20 (2024) 2305566.
[81] J.Y. Liu, M. Liu, S.B. Zheng, et al., J. Colloid Interf. Sci. 635 (2023) 284–294.
[82] Y.X. Li, J.X. Wang, S.Q. Peng, et al., Int. J. Hydrogen Energy 35 (2010) 7116–7126.
[83] L.L. Sun, X.S. Liu, X.H. Jiang, et al., J. Mater. Chem. A 10 (2022) 25279–25294.
[84] J.F. Zhu, Q.Y. Bi, Y.H. Tao, et al., Adv. Funct. Mater. 33 (2023) 2213131.
[85] H. Su, H.M. Lou, Z.P. Zhao, et al., Chem. Eng. J. 430 (2022) 132770.
[86] Y.M. Xi, W.B. Chen, W.R. Dong, et al., ACS Appl. Mater. Interfaces 13 (2021) 39491–39500.
[87] K.Y. Chen, Y.X. Shi, P. Shu, et al., Chem. Eng. J. 454 (2023) 140053.
[88] Y.X. Shi, L.L. Li, Z. Xu, et al., Chem. Eng. J. 459 (2023) 141549.
[89] R.Z. Xiong, X.X. Ke, W.F. Jia, et al., J. Mater. Chem. A 11 (2023) 2178–2190.
[90] Y.C. Wang, M.J. Liu, C.X. Wu, et al., Small 18 (2022) 2202544.
[91] Y.W. Xiao, B. Yao, M.H. Cao, et al., Small 19 (2023) 2207499.
[92] L.H. Xia, K.S. Zhang, X.D. Wang, et al., Appl. Catal. B: Environ. 325 (2023) 122387.
[93] H.Y. Liu, F. Sun, X.Y. Li, et al., Composites Part B: Eng. 259 (2023) 110746.
[94] Z.W. Zhao, Z.L. Wang, J.F. Zhang, et al., Adv. Funct. Mater. 33 (2023) 2214470.
[95] H.B. Yu, J.H. Huang, L.B. Jiang, et al., Appl. Catal. B: Environ. 298 (2021) 120618.
[96] Y.H. Peng, X.L. Guo, S.F. Xu, et al., J. Energy Chem. 75 (2022) 276–284.
[97] H.F. Li, H.T. Yu, X. Quan, et al., Adv. Funct. Mater. 25 (2015) 3074–3080.
[98] J.J. Lu, Y.H. Chen, L.N. Li, et al., Chem. Eng. J. 362 (2019) 1–11.
[99] L.L. Wang, T. Yang, L.J. Peng, et al., Chin. J. Catal. 43 (2022) 2720–2731.
[100] J.X. Bai, W.L. Chen, L. Hao, et al., Chem. Eng. J. 447 (2022) 137488.
[101] Y. Yuan, R.T. Guo, L.F. Hong, et al., Chemosphere 287 (2022) 132241.
[102] Z.J. Chen, H. Guo, H.Y. Liu, et al., Chem. Eng. J. 438 (2022) 135471.